



# Faster R-CNN, fourth-order partial differential equation and global-local active contour model (FPDE-GLACM) for plaque segmentation in IV-OCT image

Huaqi Zhang<sup>1</sup> · Guanglei Wang<sup>1</sup> · Yan Li<sup>1</sup> · Hongrui Wang<sup>1</sup>

Received: 9 July 2019 / Revised: 2 September 2019 / Accepted: 30 September 2019 / Published online: 12 October 2019  
© Springer-Verlag London Ltd., part of Springer Nature 2019

## Abstract

The accurate segmentation of plaque in intravascular optical coherence tomography (IV-OCT) image plays an important role in coronary atherosclerotic heart disease (CAD) diagnosis. To effectively provide information of coronary artery stenosis, we propose a novel hybrid framework which includes the faster R-CNN, fourth-order partial differential equation and global-local active contour model (FPDE-GLACM). This framework can efficiently detect and segment the plaque area in Speckle noise-contaminated IV-OCT images. We first detect plaque area by faster R-CNN and set bounding-box as the initial contour for active contour model. And then we minimize the joint energy functional of PDE-GLACM part to achieve the segmentation and denoising of IV-OCT images by gradient descent and finite difference scheme. Specifically, by using the Gaussian image minus original image to get the edge guide image, GLACM part obtains accurate plaque segmentation results. We perform experiments on 5000 IV-OCT images and set clinical manual segmentation results as ground truth. As expected, the results illustrate that the proposed FPDE-GLACM can provide better performance on plaque detection and segmentation. And these results may assist doctor in CAD diagnosis and treatment.

**Keywords** Plaque segmentation · Intravascular optical coherence tomography image · Faster R-CNN · Fourth-order partial differential equation · Active contour model

## 1 Introduction

Coronary atherosclerotic heart disease (CAD) [1,2] is one of the leading health problems in the world. It has characteristics of high morbidity, mortality and patients number. Acute coronary syndrome (ACS) is the most dangerous symptoms in CAD. And vulnerable plaque rupture is the main cause of ACS, which will lead to vessel blockage, myocardial ischemia and even necrosis. In CAD diagnosis, a good plaque detection and segmentation result of intravascular optical coherence tomography (IV-OCT) images can provide effective information of coronary artery stenosis and lesions for doctors. Therefore, it has great significance to propose an accurate plaque detection and segmentation approach.

In recent years, many researches have done the classification and segmentation of the vessel lumen and plaque in

IV-OCT images. They are presented in Table 1. In terms of the plaque segmentation, Athanasiou et al. [12] proposed a fully automated segmentation method based on K-means clustering. In terms of plaque classification, Athanasiou et al. [10] introduced the random forest (RF) to classify the plaque. And Gessert et al. [11] proposed deep learning based method for the classification of Cartesian and polar coordinate IV-OCT images. In Xu et al. [7,8] article, they employed the deep feature and support vector machine (SVM) to classify IV-OCT images. But reference [12] faced the problems of poor segmentation accuracy, and they [7,10] need relatively large dataset to improve accuracy. This is mainly because the uncertainty of plaque position, size, and shape in IV-OCT images.

To solve the above problems, we introduce the convolutional neural networks (CNN), which has been widely used in the detection and classification of various images and has achieved surprisingly good results. From the first application of CNN in object detection field by R-CNN [13], to the reduction of repeated computation by fast R-CNN, to the further improvement of real-time performance of target detection

✉ Guanglei Wang  
513197133@qq.com

<sup>1</sup> College of Electronic and Information Engineering, Hebei University, Baoding 071002, China

**Table 1** The comparison of IV-OCT-related works in terms of Jaccard similarity (JS) and accuracy

References	Methods	Metrics
Cheimariotis et al.'s [3]	Vessel lumen segmentation	JS = 0.844
Zahnd et al.'s [4]	Vessel lumen segmentation	JS = 0.832
Xu et al.'s [5]	Vessel lumen segmentation	JS = 0.844
Miyagawa et al.'s [6]	Vessel lumen segmentation	JS = 0.808
Xu et al.'s [7]	Plaque classification	Accuracy = 0.819
Xu's [9]	Plaque classification	Accuracy = 0.763
Cao's [8]	Plaque classification	Accuracy = 0.843
Athanasίου et al.'s [10]	Plaque classification	Accuracy = 0.856
Gessert et al.'s [11]	Plaque segmentation	JS = 0.817
Athanasίου et al.'s [12]	Plaque segmentation	JS = 0.814

algorithm by faster R-CNN [14], many improvements have been proposed to enhance the accuracy of faster R-CNN. For example, In [15], Sun et al. improved faster R-CNN framework for object detection, which includes the feature concatenation, hard negative mining, multi-scale training and model pre-training. Therefore, we consider the application of faster R-CNN-based method to detect and locate the plaque of IV-OCT images.

We know that the active contour model (ACM) has been proven to be a successful application on both nature and medical images, but it is rarely applied to plaque segmentation of IV-OCT images. At present, many improvement have been proposed to solve some limitations of the Chan–Vese (CV) [16] and local binary fitting (LBF) models [17]. In [18], Zhao et al. proposed an improved ACM in a variational level set function, which integrated the local and global intensity information of image effectively. In [19], Song et al. introduced a novel framework that employed color and texture features to delineate megakaryocytic nuclei and uses a novel dual-channel ACM to delineate its boundary. Munir et al. [20] proposed that the image convolved by a variable kernel into an energy formulation, where width of the kernel varies in each iteration. It solves the problem of detecting objects having intensity differences inside them. All these approaches improve the segmentation accuracy on images with weak edges and inhomogeneities by combining CV and LBF models, but they are more or less susceptible to initial parameters and computational complexity and sensitive to noise. Because IV-OCT image contains a large amount of Speckle noise, those methods cannot be directly used for plaque segmentation of IV-OCT images.

In addition, we need to improve the adaptability of ACM to Speckle noise. Recently, the effective denoising methods are fourth-order partial differential equation (PDE)-based methods. In [21], Srivastava et al. presented a fourth-order PDE-based nonlinear filter adapted to Speckle noise with Rayleigh distribution in IV-OCT images. And in [22], Kumar et al. also proposed a hybrid approach which contain the PDE

and fuzzy c-means (FCM) for Poisson noise removal and microbiopsy images segmentation. Moreover, PDE-based method and ACM are also implemented by minimizing the energy functional. Therefore, we take account into a new way to combine the energy function of PDE and ACM, OCT image with high level Speckle noise can be segmented.

In this paper, we propose a hybrid framework for plaque detection and segmentation in IV-OCT images based on faster R-CNN, fourth-order PDE and global-local ACM (FPDE-GLACM). Our framework employs faster R-CNN to detect the plaque location. And then PDE-GLACM is used to segment the plaque. The proposed approach is able to implement plaque segmentation and Speckle noise removal in a single process. Extensive experiments demonstrate that the proposed method has better comprehensive performance compared with other existing methods.

The rest of this paper is organized as follows. Section 2 introduces the proposed FPDE-GLACM for plaque detection and segmentation. And in Sect. 3, we present and discuss the experimental results of our approach comparison with other exciting methods. Finally, we draw conclusions in Sect. 4.

## 2 Proposed method

In this section, we introduce an automatic hybrid framework for plaque detection and segmentation in IV-OCT images. The plaque detection steps are introduced in Sect. 2.1. The contour initialization is presented in Sect. 2.2. And in Sect. 2.3, we exhibit the details of plaque segmentation.

### 2.1 The plaque detection

In image object detection, the advantages of deep learning methods have been proved. For one thing, we perform data augmentation to enrich training set, specifically in image rotate, flip and add noise. And for another, we choose faster

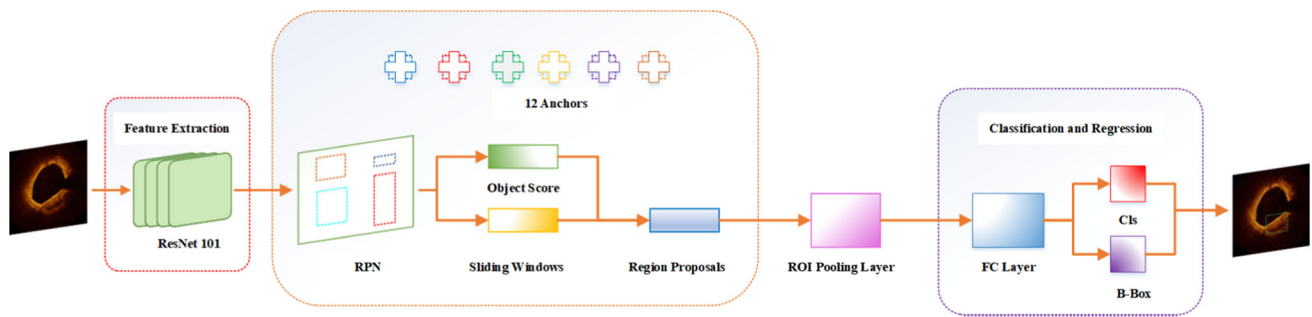


**Fig. 1** The structure of faster R-CNN

R-CNN-based method to achieve plaque detection in IV-OCT images.

Faster R-CNN consists of three parts: the feature extraction, the region proposal, the object classification and refinement. The overall structure is shown in Fig. 1.

In the first part, we introduce some typical network structure of feature extraction, which are VGG [23], GoogLeNet [24], and ResNets [25]. Considering the second part, i.e., the region proposal networks (RPN) which outputs a series of candidate regions. And traditional faster R-CNN used 9 anchors, which sometimes leads to fail recall for some irregular-shape plaques in IV-OCT images. Therefore, we introduce four scales and three aspect ratios, yielding  $k = 12$  anchors at each sliding position [15]. By default, reference frame length and width are  $(64, 64)$ ,  $(32\sqrt{2}, 64\sqrt{2})$ ,  $(64\sqrt{2}, 32\sqrt{2})$ ,  $(128, 128)$ ,  $(64\sqrt{2}, 128\sqrt{2})$ ,  $(128\sqrt{2}, 64\sqrt{2})$ ,  $(256, 256)$ ,  $(128\sqrt{2}, 256\sqrt{2})$ ,  $(256\sqrt{2}, 128\sqrt{2})$ ,  $(512, 512)$ ,  $(256\sqrt{2}, 512\sqrt{2})$ ,  $(512\sqrt{2}, 256\sqrt{2})$ . Moreover, the performance of above network structures combined with 9 and 12 anchors is discussed. And Sect. 3 lists corresponding evaluation results. From these results, we employ ResNets101 with 12 anchors as the best model for our faster R-CNN. Finally, the third part uses existing branches for classification and bounding-box regression to obtain plaque area detection result in IV-OCT images.

## 2.2 Selection of initial contour

The detection box of plaque areas was obtained by IV-OCT sequence images after using faster R-CNN. In order to further segment plaque area accurately, we introduce the initial contour of proposed FPDE-GLACM. For most methods based on ACM, a good initial contour can improve performance of segmentation. In addition, the detection box provided by faster R-CNN can effectively provide the plaque location, size and shape. It can solve the difficulty of initial contour setting due to the uncertainty of above plaque conditions. Therefore, we come up with a good choice that using faster R-CNN to provide the initial contour for PDE-GLACM. An initial contour example is shown in Fig. 2.

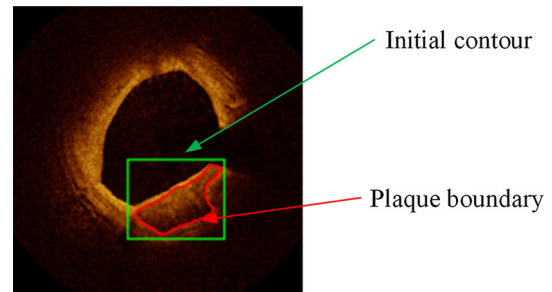


**Fig. 2** The example of initial contour (in green) and ground truth (in red) (color figure online)

## 2.3 The proposed FPDE-GLAC model

Most ACM-based methods are sensitive to noise, and IV-OCT images contain a large amount of Speckle noise. The fourth-order PDE-based method can remove noise through minimizing the objective function. Similarly, the ACM-based method also segments image by minimizing the energy functional. Therefore, we propose a hybrid segmentation model based on fourth-order PDE combined with global-local ACM, whose name is PDE-GLACM. It can segment plaque area more accurately for IV-OCT images with high-level Speckle noise. And its introduction is as follows.

Figure 3 shows the whole plaque segmentation process of proposed PDE-GLACM. To be specific, first of all, the detection result obtained by faster R-CNN is used as initial contour of PDE-GLACM. Then, we get an anisotropic diffusion image by minimizing the objective function and take it as input of Gaussian function to generate the Gaussian image. Afterward, we subtract the Gaussian image from the anisotropic diffusion image to produce the edge guide image. Moreover, we obtain the evolution image by minimizing the energy functional. Finally, for the energy functional convergence, the segmentation result is received. Instead, the evolution image is sent to PDE-GLACM to get a new anisotropic diffusion image and we will continue the above steps until it convergence.

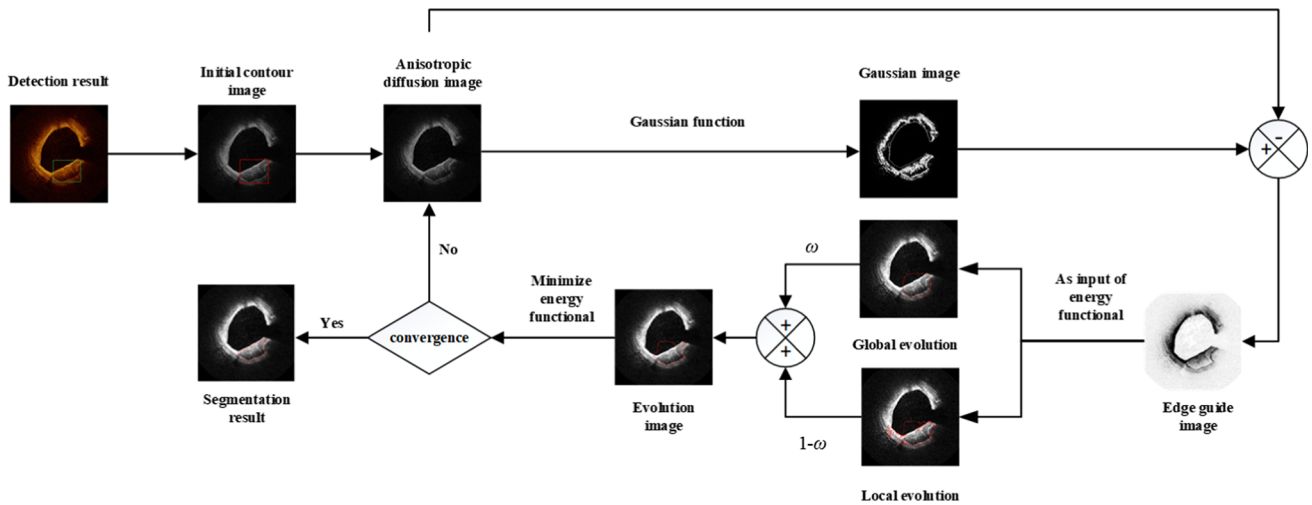


Fig. 3 The workflow of proposed FPDE-GLAC

In the first stage, we exhibit the fourth-order PDE part. It can better preserve the edge information while removing noise. IV-OCT image contains a lot of Speckle noise, and these noise follow Rayleigh distribution [21,22], it can describe as:

$$P(I|I_0) = \frac{\pi u}{2I_0^2} \exp\left(-\frac{\pi u^2}{4I_0^2}\right), \tag{1}$$

where  $I_0$  is original image and  $I$  is the restored image. And the maximum likelihood estimate of  $I_0$  can be obtained by minimizing (1)

$$L_1(I|I_0) = \ln p(I|I_0) = \ln\left(\frac{\pi I}{2I_0^2}\right) - \frac{\pi I^2}{4I_0^2}. \tag{2}$$

Then the objective function of fourth-order PDE can be defined as

$$E(I) = \int_{\Omega} \left[ L_1(I|I_0) + \lambda \zeta(\|\nabla^2 I\|) \right] d\Omega. \tag{3}$$

To remove Speckle noise in IV-OCT images, the Euler-Lagrange equation and gradient decent is used to minimize the objective function (3), and it can be rewritten as

$$\frac{\partial I}{\partial t} = \frac{\pi I^2 - 2I_0^2}{2I_0^2 I} - \lambda \nabla^2 \left[ \xi(\|\nabla^2 I\|) \nabla^2 I \right], \tag{4}$$

where diffusion coefficient  $\xi$  is defined by

$$\xi(\|\nabla^2 I\|) = \frac{1}{1 + \left(\frac{\|\nabla^2 I\|}{K}\right)^2}, \tag{5}$$

where  $K$  is given by [21]

$$K = 1.4826 \text{median}[\|\nabla I\| - \text{median}(\|\nabla I\|)]. \tag{6}$$

In the second stage, we propose the GLACM part which considers both local and global information of IV-OCT images to segment plaque area precisely. Then, we define the energy functional of GLACM as follows

$$E = \omega E^g + (1 - \omega) E^l + \mu E^p + \nu E^r, \tag{7}$$

where  $E^g$  is global energy item,  $E^l$  is local energy item,  $E^p$  is regularization item,  $E^r$  is length constraint item, and  $\omega, 1 - \omega, \mu, \nu$  are their parameters, respectively. The proposed global energy item  $E^g$  in our model is given by

$$E^g = \lambda_1 \int C_{in} |PI(x) - g_1(x)|^2 dx + \lambda_2 \int C_{out} |PI(x) - g_2(x)|^2 dx, \tag{8}$$

where  $g_1$  and  $g_2$  are the average intensities of  $PI(x)$  inside and outside of the contour  $C$ .

The edge guide image  $PI(x)$  is obtained by subtracting the anisotropic diffusion image from original image after Gaussian transformation. That is why  $PI(x)$  can clearly display plaque edge information and increase the difference between plaque and non-plaque. Using  $PI(x)$  instead of original image in CV model to drive the evolution contour  $C$  can effectively improve the segmentation effect of plaque area and avoid error segmentation. It can be defined as follows

$$PI(x) = P(x) - I(x), \tag{9}$$

where  $P(x)$  is Gaussian function.

$$P(x) = \frac{1}{\sqrt{2\pi}\sigma} \exp\left(-\frac{(I(x) - M)^2}{2\sigma^2}\right), \tag{10}$$

where  $I(x)$  is original gray image,  $M$  and  $\sigma$  are the mean and the standard deviation of pixel intensity within initial evolution contour  $C$ .

Since plaque area can reach 60–70% in initial area, the intensity mean and standard deviation of initial area are close to the intensity distribution of plaque area. Therefore, it is concluded that the larger the Gaussian value of the pixel indicates it's intensity close to the mean, which increases the possibility of being a plaque. Then, we subtract the Gaussian image from the anisotropic diffusion image to obtain the edge guide image, which has clearer plaque edge information and increases difference between plaque and non-plaques and use it as the input image to make the FPDE-GLACM more easily and accurately adhere to plaque boundaries.

The proposed local energy item  $E^1$  in our model is defined as follows: LBF model only uses original image and ignores image edge information. Thus, LBF model may cause the problem of edge leakage especially plaque segmentation in IV-OCT images. The local part of GLACM uses edge guide image instead of the original image.

$$E^1 = \lambda_1 \int \int_{C_{in}} G * |PI(x) - f_1|^2 dx dy + \lambda_2 \int \int_{C_{out}} G * |PI(x) - f_2|^2 dx dy, \tag{11}$$

where  $f_1$  and  $f_2$  are two smooth functions to approximate the neighborhood intensity of pixel  $x$ .  $G$  is the Gaussian kernel.

To improve segmentation efficiency of this model and avoid complicated level set re-initialization process, the regularization item  $E^p$  is added to the energy functional. Its expression is

$$E^p = \int \frac{1}{2} (|\nabla\varphi(x) - 1|^2) dx. \tag{12}$$

In addition, to ensure the smoothness of evolution contour, we also add the length constraint item  $E^r$  in the energy functional that is expressed as

$$E^r = \int |\nabla H(\varphi(x))| dx. \tag{13}$$

To better solve the proposed energy functional (7), we introduce the regularized Heaviside function and Dirac function:

$$H(x) = \frac{1}{2} \left[ 1 + \frac{2}{\pi} \arctan\left(\frac{x}{\varepsilon}\right) \right], \tag{14}$$

$$\delta(x) = H'(x) = \frac{1}{\pi} \frac{\varepsilon}{\varepsilon^2 + x^2}. \tag{15}$$

Then, we use level set function  $\varphi(x)$  instead of evolution curve  $C$ , by combining (14) and (15), the energy functional (7) can be rewritten as follows

$$E^{GLAC} = \mu \int \frac{1}{2} (|\nabla\varphi(x) - 1|^2) dx + \nu \int |\nabla H(\varphi(x))| dx + \omega \left\{ \lambda_1 \int |PI(x) - g_1|^2 H(\varphi(x)) dx + \lambda_2 \int |PI(x) - g_2|^2 (1 - H(\varphi(x))) dx \right\} + (1 - \omega) \left\{ \lambda_1 \int \int G * |PI(x) - f_1|^2 H(\varphi(x)) dx dy + \lambda_2 \int \int G * |PI(x) - f_2|^2 (1 - H(\varphi(x))) dx dy \right\} \tag{16}$$

Using the variation method, expressions of  $g_i$  and  $f_i$  can be obtained by

$$g_1 = \frac{\int PI(x) H(\varphi(x)) dx}{\int H(\varphi(x)) dx}, \tag{17}$$

$$g_2 = \frac{\int PI(x) (1 - H(\varphi(x))) dx}{\int (1 - H(\varphi(x))) dx}, \tag{18}$$

$$f_1 = \frac{G * [PI(x) H(\varphi(x))]}{G * H(\varphi(x))}, \tag{19}$$

$$f_2 = \frac{G * [PI(x) (1 - H(\varphi(x)))]}{G * (1 - H(\varphi(x)))}. \tag{20}$$

According to the Euler–Lagrange equation and gradient descent method, the evolution function of level set function  $\varphi(x)$  can be obtained as follows

$$\frac{\partial\varphi}{\partial t} = \mu \left( \nabla^2\varphi - \operatorname{div} \left( \frac{\nabla\varphi}{|\nabla\varphi|} \right) \right) + \nu \delta(\varphi) \operatorname{div} \left( \frac{\nabla\varphi}{|\nabla\varphi|} \right) + \delta(\varphi) (e_1 + e_2). \tag{21}$$

The expressions of  $e_1$  and  $e_2$  are

$$e_1 = \omega_1 \left[ -\lambda_1 |PI(x) - g_1|^2 + \lambda_2 |PI(x) - g_2|^2 \right], \tag{22}$$

$$e_2 = \omega_2 \left[ -\lambda_1 \int \int G * |PI(x) - f_1|^2 dx dy + \lambda_2 \int \int G * |PI(x) - f_2|^2 dx dy \right]. \tag{23}$$

The solution of evolution function (21) can be achieved by finite difference method

$$\begin{aligned} \frac{\varphi_{ij}^{n+1} - \varphi_{ij}^n}{\Delta t} &= \mu \left( \nabla^2 \varphi_{ij}^n - \operatorname{div} \left( \frac{\nabla \varphi_{ij}^n}{|\nabla \varphi_{ij}^n|} \right) \right) \\ &+ \nu \delta \left( \varphi_{ij}^n \right) \operatorname{div} \left( \frac{\nabla \varphi_{ij}^n}{|\nabla \varphi_{ij}^n|} \right) + \delta(\varphi_{ij}^n)(e_1 + e_2). \end{aligned} \tag{24}$$

Finally, the expression of proposed FPDE-GLACM is defined as follows

$$\begin{aligned} \frac{\partial I_{ij}}{\partial t} &= \frac{I_{ij}^{n+1} - I_{ij}^n}{\Delta t} \\ &= \left\{ \frac{\pi I_{ij}^2 - 2I_0^2}{2I_0^2 I_{ij}} - \lambda \nabla^2 \left[ \xi(|\nabla^2 I_{ij}|) \nabla^2 I_{ij} \right] \right. \\ &\quad \left. + \operatorname{arg\,min} E^{GLAC} \right\} \end{aligned} \tag{25}$$

And (25) can be rewritten as

$$\begin{aligned} I_{ij}^{n+1} &= I_{ij}^n \\ &+ \Delta t \left\{ \frac{\pi I_{ij}^2 - 2I_0^2}{2I_0^2 I_{ij}} - \lambda \cdot \nabla^2 \left[ \xi(|\nabla_{ij}^2 I_{ij}|) \nabla_{ij}^2 I_{ij} \right] \right. \\ &\quad \left. + \operatorname{arg\,min} E^{GLAC} \right\} \end{aligned} \tag{26}$$

### 3 Experiments

In this section, to demonstrate the effectiveness of the proposed FPDE-GLACM, we use both synthetic images and IV-OCT images to evaluate its performance through extensive experiments. The experimental data include synthetic image and 5000 IV-OCT images which contain training dataset (4000) and testing dataset (1000). The size of IV-OCT image is 300 × 300 pixels. These images were collected by a C7 model IV-OCT scanner (St. Jude Medical, USA), which was provided by the department of cardiology at Peking Union Medical College Hospital, China. And the experimental environment is Intel Core i7-8750H CPU, NVIDIA GeForce GTX 1070 GPU, 16.00 GB DDR4 memory, Windows 10 operating system, Python 3.6.1, and MATLAB 2018a software.

#### 3.1 Evaluation of plaque detection

In this section, selection of CNN model is discussed, and accuracy of performance of faster R-CNN is evaluated. The

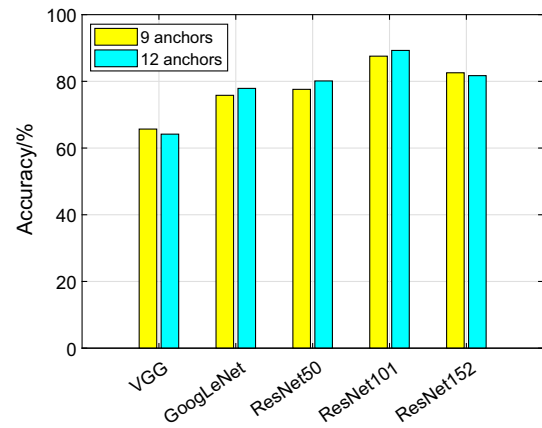


Fig. 4 Accuracy of VGG, GoogLeNet, ResNet50, ResNet101, and ResNet152 with 9 and 12 anchors, respectively

accuracy can calculate the proportion of correctly classification, which is defined as

$$\text{Accuracy} = \frac{\text{TP} + \text{TN}}{\text{TP} + \text{TN} + \text{FP} + \text{FN}}, \tag{27}$$

where TP, TN, FP, and FN are the true positive, true negatives, false positive, and false negatives, respectively.

The performance of applying VGG, GoogLeNet, and ResNet to faster R-CNN was compared and shown the results in Fig. 4. It can be found that ResNet has the highest accuracy. Hence, we choose ResNet in feature extraction. Then, we test three well-known structures of ResNet which namely ResNet50, ResNet101, and ResNet152 and compared their accuracy when choosing 9 anchors and 12 anchors respectively. As also shown in Fig. 4, the ResNet101 combined with 12 anchors is the best choice. Therefore, we use the ResNet101 combined with 12 anchors to construct faster R-CNN and use it to implement the plaque detection for IV-OCT images.

#### 3.2 The segmentation evaluation

To more accurately and objectively evaluate the proposed framework performance, we select synthetic images and IV-OCT images for experiments and use manual segmentation results of doctors as ground truth and two metrics as the evaluation standard, which are Jaccard similarity (JS) and Dice similarity coefficient (DICE). To test the segmentation accuracy of the proposed FPDE-GLACM and other existing methods, the JS is introduced to evaluate the similarity between algorithm segmentation results and ground truth, which is represented by

$$\text{JS} = \frac{|A \cap B|}{|A \cup B|}, \tag{28}$$

where  $A$  is the algorithm segmentation result and  $B$  is ground truth.

Then, we also use the DICE to quantitatively evaluate the above methods performance and the DICE is defined by

$$\text{DICE} = \frac{2|A \cap B|}{|A| + |B|}, \quad (29)$$

where  $A$  is the algorithm segmentation result and  $B$  is ground truth. Similarly, the closer the values to 1 of JS and DICE mean the better segmentation effects are achieved.

### 3.2.1 Experiment with synthetic images

To test the performance of proposed FPDE-GLACM in synthetic images with different level Speckle noise, we compare it with improved active contour model (IACM) [18] and dual-channel active contour (DCAC) model [19]. The results are shown in Fig. 5. For above approaches, the same iterations are used. Note that FPDE-GLACM provides better performance than IACM and DCAC, mainly because the energy functional of FPDE-GLACM fuse the objective function based on Rayleigh distribution and fourth-order PDE to avoid noise interference and employ edge guide image to retain the edge information of synthetic images.

To test the performance of a model only visual comparison is not enough and the segmentation results need to be evaluated by JS and DICE. The results are shown in Fig. 6. It is obvious that FPDE-GLACM is used to segment synthetic images with different levels Speckle noise with high precision. Besides, with the increase in noise, the segmentation precision of each algorithm decreases, especially IACM, which is sensitive to Speckle noise. Therefore, we can conclude that the FPDE-GLACM can achieve better segmentation results compared to above-mentioned methods for synthetic images with different levels of Speckle noise.

### 3.2.2 Experiment with IV-OCT images

In the experiment with IV-OCT images, we compared the performance between the proposed method and some classical methods such as the regional growth (RG) [26], graph cut (GC) [27], random walk (RW) [28], local binary fitting (LBF) model [17], and some advanced methods such as improved active contour model (IACM) [18], dual-channel active contour (DCAC) model [19] combined with the faster R-CNN. In the following, we call them CNN-RG, CNN-GC, CNN-RW, CNN-LBF, CNN-IACM, and CNN-DCAC, respectively. The corresponding results are shown in Fig. 7. It is found that CNN-RG segment almost areas with high intensity and sensitive to noise, so it cannot effectively segment plaque of IV-OCT images. CNN-GC and CNN-RW can roughly segment plaque area, but their accuracy is relatively

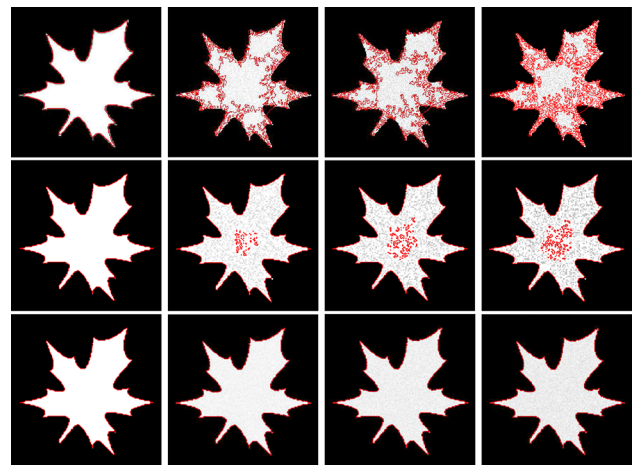


**Fig. 5** Segmentation comparison, from the first to last rows are IACM, DCAC, and FPDE-GLACM with 0%, 1%, 2%, and 3% Speckle noise, respectively

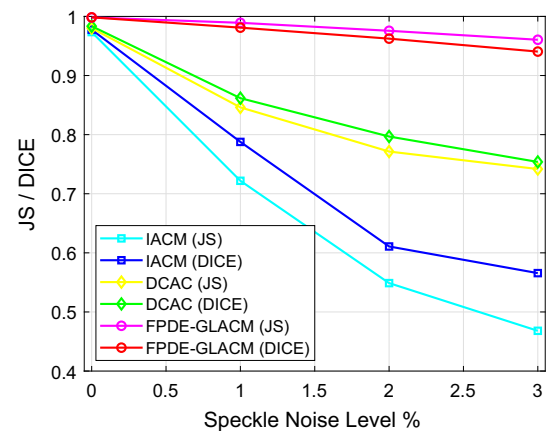


**Fig. 6** JS and DICE of synthetic image

unsatisfied. Because CNN-LBF is sensitive to noise, it has the worst segmentation results among the above four ACM-based methods. CNN-IACM and CNN-DCAC can obtain relatively better segmentation results at most plaque edge, but there have some over-segmentation near plaque edge between vessel lumen. From visual effect, it can be observed that the proposed FPDE-GLACM has the highest accuracy in plaque segmentation of IV-OCT images.

In order to quantitatively evaluate the performance of above seven methods, mean and variance value of JS and DICE are illustrated in Table 2. We observe that the proposed FPDE-GLACM attains better performance than other six methods. The JS and DICE of our method reach  $0.851 \pm 0.042$  and  $0.876 \pm 0.043$ , respectively.

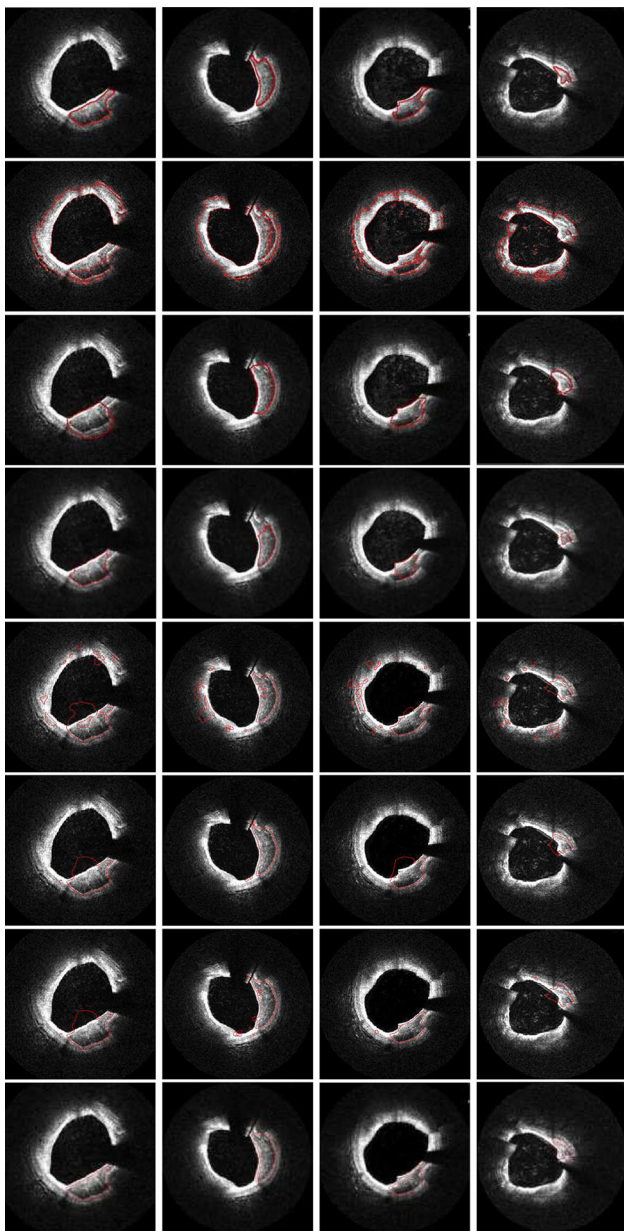


**Fig. 7** Segmentation results for IV-OCT images. From the first to the last row are ground truth, CNN-RG, CNN-GC, CNN-RW, CNN-LBF, CNN-IACM, CNN-DCAC, and FPDE-GLACM, respectively

**Table 2** JS and DICE obtained by seven methods

Methods	JS	DICE
CNN-RG	$0.348 \pm 0.092$	$0.403 \pm 0.107$
CNN-GC	$0.520 \pm 0.061$	$0.554 \pm 0.082$
CNN-RW	$0.618 \pm 0.054$	$0.659 \pm 0.051$
CNN-LBF	$0.615 \pm 0.062$	$0.621 \pm 0.059$
CNN-IACM	$0.742 \pm 0.058$	$0.803 \pm 0.034$
CNN-DCAC	$0.721 \pm 0.051$	$0.744 \pm 0.043$
FPDE-GLACM	$0.851 \pm 0.042$	$0.876 \pm 0.043$

## 4 Conclusions

In this paper, we propose a hybrid framework based on the faster R-CNN and PDE-GLACM. The framework first detects plaque area in IV-OCT images by using faster R-CNN. Secondly, we use the detection box as the initial contour of PDE-GLACM. And then, to effectively remove Speckle noise, we combine the Rayleigh distribution with fourth-order PDE and add its objective function to the energy functional of proposed GLACM which considers global and local information of image. It can effectively overcome the influence of Speckle noise and realize the segmentation of plaque area in IV-OCT images. The proposed framework obtains accurate detection and segmentation result compared with other existing methods, and these results may assist doctor in diagnosis and treatment of CAD. In further research, we will concentrate on improving this framework for computational complexity.

**Acknowledgements** This work was supported by the projects of the Natural Science Foundation of Hebei Province (F2015201196), Science and Technology Research Program (QN2015135), Key Natural Science Foundation (F2017201222) and Youth Fund Projects (QN2014101) of the Hebei Province Department of Education, China.

## References

1. Benjamin, E.J., Virani, S.S., Callaway, C.W., et al.: Heart disease and stroke statistics 2018 update: a report from the American Heart Association. *Circulation* **137**, e67–e492 (2018)
2. Kume, T., Uemura, S.: Current clinical applications of coronary optical coherence tomography. *Cardiovasc. Interv. Ther.* **33**, 1–10 (2018)
3. Cheimariotis, G., Chatzizisis, Y.S., Koutkias, V., et al.: ARC-OCT: automatic detection of lumen border in intravascular OCT images. *Comput. Methods Progr. Biomed.* **1**, 21–32 (2017)
4. Zahnd, G., Hoogendoorn, A., Combaret, N., et al.: Contour segmentation of the intima, media, and adventitia layers in intracoronary OCT images: application to fully automatic detection of healthy wall regions. *Int. J. Comput. Assist. Radiol. Surg.* **12**, 1923–1936 (2017)
5. Xu, M., Cheng, D.W.J., et al.: Graph based lumen segmentation in optical coherence tomography images. In: *Proceedings of IEEE Information, Communications and Signal Processing (ICSP)*, pp. 1–5 (2015)
6. Miyagawa, M., Costa, M.G.F., Gutierrez, M.A., et al.: Lumen segmentation in optical coherence tomography images using convolutional neural network. In: *Proceedings of IEEE Engineering in Medicine and Biology Society (EMBC)*, pp. 600–603 (2018)
7. Xu, M., Cheng, J., Wong, D.W.K., et al.: Automatic image classification in intravascular optical coherence tomography images. In: *Proceedings of IEEE Region 10 Conference (TENCON)*, pp. 11–22 (2016)
8. Cao, Y., Jin, Q., Chen, Y., et al.: Automatic identification of side branch and main vascular measurements in intravascular optical coherence tomography images. In: *Proceedings of IEEE International Symposium on Biomedical Imaging (ISBI)*, pp. 608–611 (2017)



9. Xu, M., Cheng, J., Li, A., et al.: Fibroatheroma identification in intravascular optical coherence tomography images using deep features. In: Proceedings of IEEE Engineering in Medicine and Biology Society (EMBC), pp. 1501–1504 (2017)
10. Athanasiou, L., Karvelis, P.S., Tsakanikas, V., et al.: A novel semi-automated atherosclerotic plaque characterization method using grayscale intravascular ultrasound images: comparison with virtual histology. *IEEE Trans. Inf. Technol. Biomed.* **16**, 391–400 (2011)
11. Gessert, N., Lutz, M., Heyder, M., et al.: Automatic plaque detection in IV-OCT pullbacks using convolutional neural networks. *IEEE Trans. Med. Imaging* **38**, 426–434 (2018)
12. Athanasiou, L., Bourantas, C., Rigas, G., et al.: Methodology for fully automated segmentation and plaque characterization in intracoronary optical coherence tomography images. *J. Biomed. Opt.* **17**(2), 568–580 (2014)
13. Girshick, R., Donahue, J., Darrell, T., et al.: Rich feature hierarchies for accurate object detection and semantic segmentation. In: Proceeding of IEEE Computer Vision and Pattern Recognition (CVPR), pp. 580–587 (2014)
14. Ren, S., He, K., Girshick, R., et al.: Faster R-CNN: towards real-time object detection with region proposal networks. *IEEE Trans. Pattern Anal. Mach. Intell.* **39**, 1137–1149 (2017)
15. Sun, X., Wu, P., Hoi, S.C.H.: Face detection using deep learning: an improved faster R-CNN approach. *Neurocomputing* **299**, 42–50 (2017)
16. Chan, T.F., Vese, L.A.: Active contours without edges. *IEEE Trans. Image Process.* **1**, 266–277 (2001)
17. Li, C., Kao, J.C.G.C., et al.: Minimization of region-scalable fitting energy for image segmentation. *IEEE Trans. Image Process.* **17**, 1940–1949 (2008)
18. Zhao, W., Xu, X., Zhu, Y., et al.: Active contour model based on local and global gaussian fitting energy for medical image segmentation. *Int. J. Light Electron Opt.* **158**, 1160–1169 (2018)
19. Song, T., Sanchez, V., EIDaly, H., et al.: Dual-channel active contour model for megakaryocytic cell segmentation in bone marrow trephine histology images. *IEEE Trans. Biomed. Eng.* **64**, 2913–2923 (2017)
20. Munir, A., Soomro, S., Lee, C.H., et al.: Adaptive active contours based on variable kernel with constant initialisation. *IEEE Trans. Image Process.* **12**, 1117–1123 (2018)
21. Srivastava, S., Srivastava, R., Sharma, N., et al.: A fourth-order PDE-based non-linear filter for speckle reduction from optical coherence tomography images. *Int. J. Biomed. Eng. Technol.* **10**, 59–69 (2012)
22. Kumar, R., Srivastava, S., Srivastava, R.: A fourth order PDE based fuzzy c-means approach for segmentation of microscopic biopsy images in presence of Poisson noise for cancer detection. *Comput. Methods Progr. Biomed.* **146**, 59–68 (2017)
23. Simonyan, A.Z.K.: Very deep convolutional networks for large-scale image recognition. In: Proceeding of Learning Representations (ICLR), pp. 1–14 (2015)
24. Szegedy, C., Liu, W., Jia, Y., Sermanet, P., Reed, S., Anguelov, D., Erhan, D., Vanhoucke, V., Rabinovich, A.: Going deeper with convolutions. In: Proceeding of IEEE Conference on Computer Vision and Pattern Recognition (CVPR), pp. 1–9 (2015)
25. He, K., Zhang, X., Ren, S., et al.: Deep residual learning for image recognition. In: Proceeding of IEEE Computer Vision and Pattern Recognition (CVPR), pp. 770–778 (2016)
26. Jin, S., Su, Y., Gao, S., et al.: Deep learning: individual maize segmentation from terrestrial lidar data using faster R-CNN and regional growth algorithms. *Front. Plant Sci.* **9**, 866 (2018)
27. Salah, M.B., Mitiche, A., Ayed, I.B., et al.: Multiregion image segmentation by parametric kernel graph cuts. *IEEE Trans. Image Process.* **20**, 545–557 (2011)
28. Fechter, T., Adebahr, S., Baltas, D., et al.: Esophagus segmentation in CT via 3D fully convolutional neural network and random walk. *Med. Phys.* **44**, 6341–6352 (2017)

**Publisher's Note** Springer Nature remains neutral with regard to jurisdictional claims in published maps and institutional affiliations.